# V5 Spin Transport in Magnetic Nanostructures

Daniel E. Bürgler
Peter Grünberg Institut
Elektronische Eigenschaften (PGI-6)
Forschungszentrum Jülich GmbH
Email: D.Buergler@fz-juelich.de

## Contents

# 1 Introduction

In conventional electronic devices the charge of electrons is used to realize certain functionalities by controlling electric currents for example by electric fields. Therefore, the conventional electronics bases on charge-transport. The spin is a further fundamental property of electrons. The electronic spins correspond to magnetic moments, which give rise to the magnetism of solids. On the other hand, the spin also provides a means to act with spin-dependent influences (*e.g.* a magnetic field or spin-dependent scattering) on the electrons and their motion. In contrast to the electric charge of an electron, which is always negative and conserved, the spin degree of freedom can adopt two orientations with respect to a given quantization axis, spin-up and spin-down. In a system with an imbalance of the two spin orientations (*e.g.* a ferromagnetic material) *spin-transport* is associated with an electrical current. In this context, one defines the spin polarization of the current by

$$P = \frac{I^{\uparrow} - I^{\downarrow}}{I^{\uparrow} + I^{\downarrow}}, \tag{1}$$

where $I^{\uparrow(\downarrow)}$ denotes the current due to spin-up (spin-down) electrons. $|P| = 100\%$ indicates a completely polarized current, whereas $P = 0$ corresponds to an unpolarized current with no associated spin-transport. Transport effects and electronic devices that take advantage of the spin degree of freedom of the electron to achieve new functionalities constitute the field called "*spintronics*" (or "*magnetoelectronics*").
For electrons in a solid-state environment, an imprinted spin polarization $\Delta P$ is in general not conserved. The spin can be flipped for instance by electron-electron interaction or spin-flip scattering from magnetic impurities. The characteristic length scale for spin-transport in a solid, within which $P$ is conserved, is the spin diffusion (or spin-flip) length $\lambda$ defined by

$$\Delta P(x) = \Delta P_0 \exp(-\frac{x}{\lambda}), \tag{2}$$

where $\Delta P_0$ is the initial, imprinted spin polarization at the position $x = 0$. The value of $\lambda$ is material-dependent and varies in the range from a few nanometers (*e.g.* $Ni_{80}Fe_{20}$ alloy, also called permalloy) up to several tens of nanometers (*e.g.* Co) for magnetic alloys and metals and exceeds 100 nm for non-magnetic metals (*e.g.* Cu). $\lambda$ also depends on extrinsic properties like crystallinity and purity of the material. Much higher values exceeding 100 $\mu$m have been demonstrated in bulk GaAs [1]. But in most cases –in particular those dealing with elemental metals and their alloys– spin-transport only persists over distances of the order of a few nanometers. For this reason *layered structures* with individual layer thicknesses of the order of a few nanometers play a crucial role for spin-transport effects. The interfaces between neighboring layers additionally give rise to spin-dependent reflection, transmission, and scattering.
The main focus of this lecture is on the spin-transport effects *giant magnetoresistance* (GMR) and *spin-torque transfer* (STT). The latter gives rise to current-induced magnetization switching and current-driven magnetization dynamics. For each of these effects a description of the phenomenon and a physical picture of the basic mechanisms will be given.

# 2 Giant magnetoresistance (GMR)

GMR has been discovered simultaneously and independently in 1988 by Peter Grünberg in Jülich and Albert Fert in Paris. In 2007, they have been awarded the Nobel Prize in physics for

their discovery, which is the cornerstone of spintronics. The fascinating new physics and the high relevance for applications – for instance in read heads of hard-disk drives and in magnetic random access memory (MRAM) devices– has triggered enormous research efforts in this field and led to further discoveries and developments such as the spin-torque transfer effects to be discussed in Sect. 3.

## 2.1 Phenomenological description

We consider layered magnetic structures comprised of ferromagnetic layers separated by non-ferromagnetic, metallic spacers. The giant magnetoresistance effect describes the finding that the electric resistivity depends on the relative alignment of the magnetizations of adjacent ferromagnetic layers [2]. If we denote by $R_P$ the resistance for parallel alignment of adjacent ferromagnetic films and by $R_{AP}$ the same for antiparallel alignment, then the strength of GMR is usually quoted in terms of

$$\frac{\Delta R}{R_P} = \frac{R_{AP} - R_P}{R_P}. \tag{3}$$

Mostly, the resistance is highest for antiparallel alignment yielding a positive $\frac{\Delta R}{R_P}$. This situation corresponds to the so-called *normal* GMR effect. In trilayers consisting of only two ferromagnetic layers separated by a non-ferromagnetic spacer layer, the GMR ratio $\frac{\Delta R}{R_P}$ can reach values of up to 36% at RT, whereas multilayers with many repetitions of ferromagnetic/non-ferromagnetic bilayers yield GMR ratios of up to 80%.

The first experiments showing the GMR effect have been performed independently and simultaneously by Peter Grünberg [3] in Jülich and Albert Fert [4] at the university Paris-Sud using Fe/Cr/Fe trilayers or Fe/Cr multilayers, respectively. The pioneering results are displayed in Fig. 1. At zero field adjacent Fe layers align antiparallel due to the antiferromagnetic interlayer exchange coupling, which was discovered by Peter Grünberg in 1986 [5]. Interlayer exchange coupling results from an indirect exchange interaction between two ferromagnetic layers, which is mediated by the conduction electrons of a thin non-ferromagnetic spacer layer (Cr in the Fe/Cr/Fe structures). Depending on the spacer thickness, the interaction is ferromagnetic and leads to a parallel alignment of adjacent ferromagnetic layer magnetizations or it is

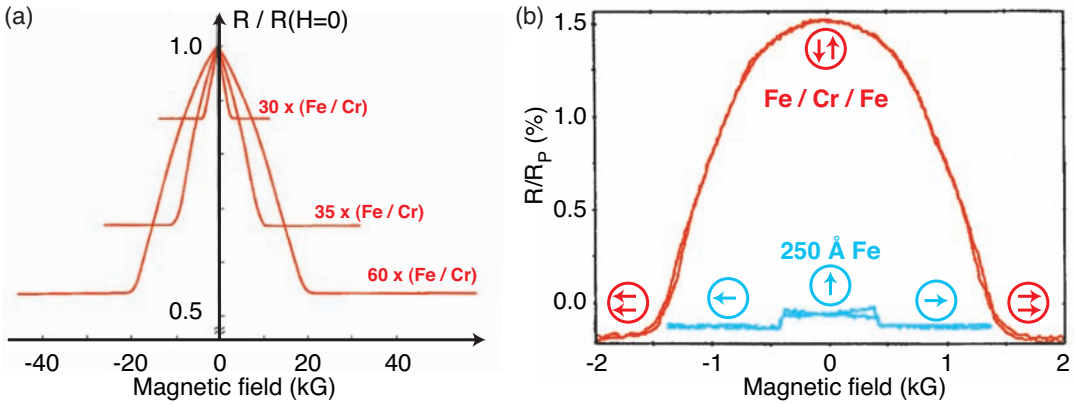


**Fig. 1:** *First observations of the GMR effect in (a) Fe/Cr multilayers [4] and (b) Fe/Cr/Fe trilayers [3]. The blue curve in (b) shows the AMR effect of a single Fe film with a thickness equal to the total Fe thickness in the trilayer.*

antiferromagnetic and favors the antiparallel alignment. In the present context, the antiferromagnetic interlayer coupling is of interest, because it allows one to reversibly switch between the antiparallel configuration at zero field and the parallel alignment in a sufficiently high, saturating external magnetic field [see arrows in Fig. 1(b)]. The transition from the antiparallel to the parallel alignment is accompanied by a drastic change of the resistivity. The blue curve in Fig. 1(b) shows for comparison the anisotropic magnetoresistance effect (AMR) of a 250 Å-thick Fe layer. This thickness is equal to the total Fe thickness in the trilayer. AMR describes the dependence of the electric resistivity on the angle between the current and the magnetization direction. AMR is a volume effect discovered in 1857 and was applied in read heads in the 1990's before the invention of GMR read heads. The much larger response of the layered structures is the reason why the new effect was dubbed *giant* magnetoresistance (GMR).

Antiferromagnetic interlayer exchange coupling is not a necessary condition to observe the GMR effect. The antiparallel alignment at small fields can also be achieved by hysteresis effects. For instance, one can choose two ferromagnetic materials with clearly different coercive fields $H_c^{(1)} < H_c^{(2)}$. After a field reversal layer 1 will remagnetize in the direction of the external field at $H_c^{(1)}$. It is then antiparallel aligned to layer 2 up to the field $H_c^{(2)}$, where layer 2 also remagnetizes to align with the applied field. Another possibility is to magnetically pin one ferromagnetic layer by the exchange bias effect due to the contact with an antiferromagnet, whereas the magnetization of the second ferromagnetic layer is free to rotate when an external field is applied. An example is shown in Fig. 2. Such arrangements are called *spin-valves* and are relevant for applications. The exchange bias effect shifts the hysteresis curves of a ferromagnetic layer in contact with an antiferromagnet on the field axis due to the direct exchange

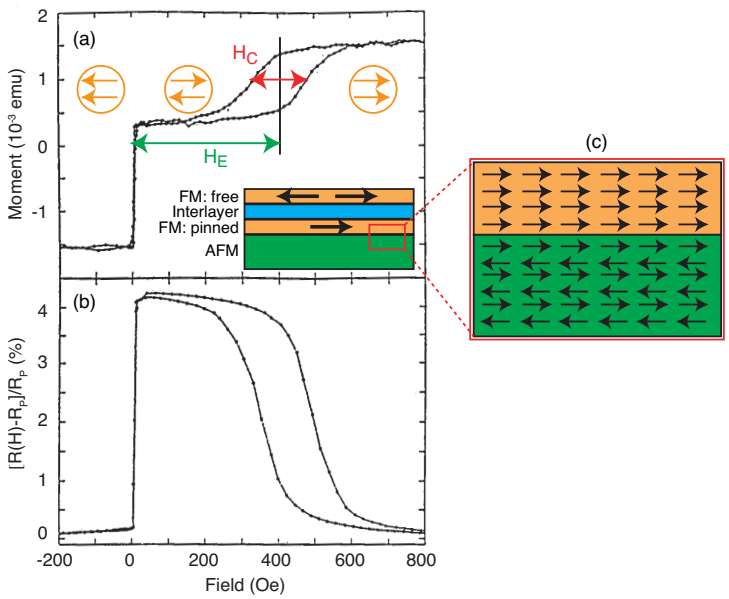


**Fig. 2:** *(a) Hysteresis loop $M(H)$, and (b) giant magnetoresistance $[R(H) - R_P]/R_P$ of a $Ni_{80}Fe_{20}$ (6 nm)/Cu (2.2 nm)/$Ni_{80}Fe_{20}$ (4 nm)/FeMn (7 nm) GMR spin-valve at RT (after Ref. [6].) The spin-valve structure is schematically shown in the inset of (a). Pairs of arrows indicate the relative alignment of the magnetizations of the magnetic films when the field is increased from negative to positive values. (c) Microscopic view of an idealized ferromagnet/antiferromagnet interface.*

**Table 1:** *Representative values for GMR ratios. Geometry is CIP unless specially marked with CPP (see text). Auxiliary layers, which are not directly active for the GMR effect, are mostly omitted. Numbers in brackets indicate the layer thickness in Å. Compiled from Ref. [8].*

| Sample | $\Delta R/R_P(\%)$ | Temperature (K) |
|---|---|---|
| $[$Fe(4.5)/Cr(12)$]_{50}$ | 220 | 1.5 |
| | 42 | 300 |
| $[$Co(10)/Cu(10)$]_{100}$ | 80 | 300 |
| Co(30)/Cu(19)/Co(25) | 19 | 300 |
| $Co_{90}Fe_{10}$(40)/Cu(25)/$Co_{90}Fe_{10}$(8)... | 7 | 300 |
| NiFe(100)/Cu(25)/Co(22) | 4.6 | 300 |
| ...CoFe/AgCu(15)/CoFe... | 4–7 | 300 |
| $[$Co(15)/Cu(12)$]_n$ CPP | 170 | 4.2 |
| $[$Co(12)/Cu(11)$]_{180}$ CPP | 55 | 300 |
| $Co_2$MnSi/Ag/$Co_2$MnSi CPP [9] | 67 | 110 |
| | 36 | 300 |

interaction between the surface spins of the antiferromagnet and the magnetization of the ferromagnetic film [Fig. 2(c)]. As a result the hysteresis curve of the pinned layer in Fig. 2(a) is shifted to positive fields by the so-called exchange bias field $H_E$. The free permalloy layer remagnetizes in small fields. Its coercivity is so small that it cannot be resolved in Figs. 2(a) and (b). The rather wide hysteresis loop [large coercivity $H_C$ in Fig. 2(a)] of the pinned film is associated with the exchange bias effect. Figure 2(b) shows the corresponding GMR signal. The steep slope of the resistance near zero field provides a sensitive signal to measure small magnetic fields.

The GMR effect can be measured in two different geometries, namely the CIP (current-in-plane) and the CPP (current-perpendicular-plane) geometry. The relative effect is stronger in the CPP geometry. However, due to the extremely unfavorable geometric conditions (lateral dimensions some orders of magnitude larger than the film thickness) the voltage drop perpendicular to the layers is extremely small. Typical resistance times area products $RA$ are of the order of $10^{-4}$ $\Omega\mu$m$^2$. The resulting very small resistances are not measurable because they get lost in lead and contact resistances. Lateral pattering on the sub-$\mu$m scale or superconducting leads are required to obtain structures with measurable resistances. On the other hand, CPP-GMR in suitably structured devices can become sufficiently strong to be of interest for applications, *e.g.* GMR-based magnetic random-access memories (MRAM) [7]. Representative and record values for the GMR effect as defined by Eq. (3) both in the CIP and CPP geometry are compiled from the literature in Table 1.

## 2.2 Microscopic picture: Spin-dependent scattering

The mechanism leading to GMR can be understood within Mott's two current model [2, 10], which assumes two independent current channels for spin-up and spin-down electrons. Due to their Fermi velocity the conduction electrons propagate with high speed but arbitrary direction through the layered structure. A current results from a much smaller drift velocity in the direction of the applied electric field. Therefore, the schematic representation and the substitutional

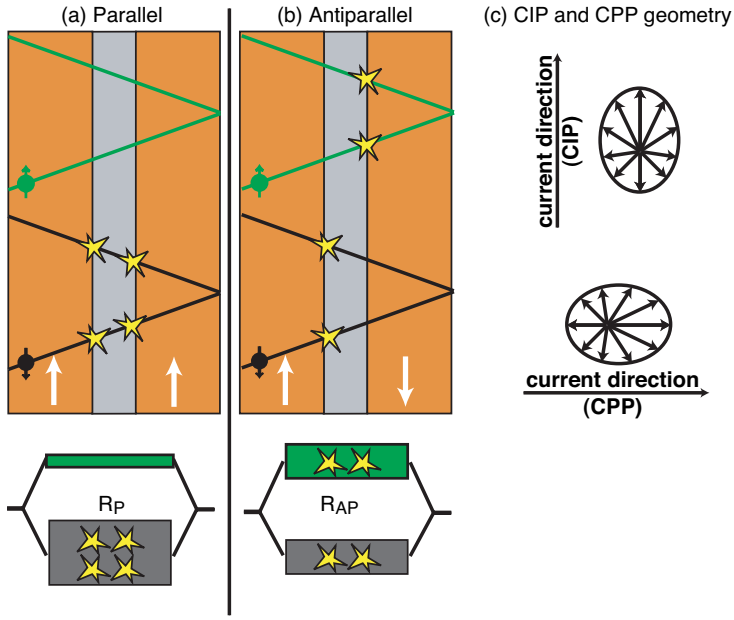


**Fig. 3:** *Simplified picture of spin-dependent scattering for the explanation of the GMR effect. Only minority electrons are scattered as schematically indicated by the stars. Majority electrons are not scattered and cause a short-circuit effect, which appears for parallel alignment of the magnetizations (a) but not for antiparallel alignment (b). The substitutional circuit diagrams in the lower part for the total resistivities, $R_P$ and $R_{AP}$, yield the relation $R_P < R_{AP}$ and hence the GMR effect. (c) Schematic electron velocity distributions for CIP and CPP geometry.*

circuit diagrams in Fig. 3 hold for both CIP and CPP geometry as indicated by the schematic spatial velocity distribution in Fig. 3(c).

In Figs. 3(a) and (b) electron paths between two reflections at outer surfaces are shown with scattering events in between. In order not to confuse the picture the changes in direction due to the scattering events are suppressed. The scattering processes are the cause of electric resistance. Only states near the Fermi energy contribute to the electric conductivity because they can reach empty final states just above the Fermi energy after a scattering event. In order to demonstrate how spin-dependent scattering leads to the GMR effect, we use in the following a simple –albeit unrealistic– consideration, whose main argument is nevertheless valid in reality: In Fig. 3 it is assumed that only minority electrons (spin antiparallel to the local magnetization) are scattered at the magnetic/non-magnetic interfaces. Thus, for parallel alignment of the magnetizations [Fig. 3(a)], majority electrons are not scattered at all, leading to a short-circuit ($R = 0$) of the associated current. Therefore, the resistivity for the total current vanishes, too, as can be seen in the lower part of Fig. 3(a), where the two spin channels are represented by two resistors in parallel connection. For antiparallel alignment of the magnetizations [Fig. 3(b)] there are scattering events for both types of electrons. Hence, the resistivity for the total current is finite. It is clear that even if the above strict condition is relaxed, the resistivity can be higher for antiparallel alignment compared to the parallel one. The GMR effect can only be observed when electrons from one ferromagnetic layer reach the other one without loosing their spin orientation. This condition results in two different limitations for the two measurement geometries shown in Fig. 3(c). For the CIP geometry the electron mean free path determines the “width” of the band within which an electron diffuses parallel to the interfaces. The spacer layer must be

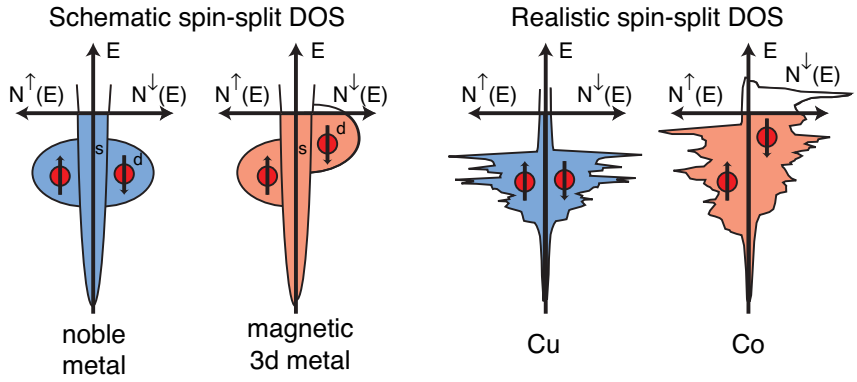


**Fig. 4:** *(a) Schematic spin-split density of states (DOS) for a noble metal and a 3d transition metal representing the spacer and magnetic layer, respectively. The exchange splitting in the ferromagnet gives rise to different DOS at the Fermi level for spin-up and spin-down states ($N^{\uparrow} \neq N^{\downarrow}$). (b) Realistic spin-split DOS for Cu and Co show qualitatively the same features as depicted in (a).*

thinner than the mean free path, otherwise an electron starting from one ferromagnet will undergo a momentum scattering process (change of momentum direction without spin-flip) before it reaches the other ferromagnet. As momentum scattering processes have a higher probability than spin-flip scattering, the mean free path is shorter than the spin diffusion length $\lambda$. Thus, CIP-GMR requires spacer thicknesses of just a few nanometers. For the CPP geometry, however, the drift velocity due to the applied bias voltage makes sure, that the electrons propagate –possibly undergoing several momentum scattering events– from one ferromagnetic layer to the other. Here, the spacer layer must be thinner than $\lambda$ in order to conserve the spin of the electrons while they cross the spacer. An animation explaining this simple picture of GMR and how GMR is used in read heads of high-density hard-disks is available on the internet [11].
The origin of the spin-dependent behavior assumed in Fig. 3 can be found in the spin-split density of states (DOS) of 3d transition metals (Fig. 4). It shows different numbers of final states (density of states near the Fermi energy) for majority and minority electrons and hence different spin-dependent scattering probabilities.

## 2.3 Application of GMR

The application of the GMR effect in read heads of hard-disk drives (HDD) is currently the most important one in terms of market volume. GMR-based read heads were first introduced 1997 by IBM. The advantage of GMR over AMR, which has been used since the early 1990's, is not only the larger signal [see Fig. 1(b)] but also the fact that GMR in contrast to AMR is predominantly an interface effect. This allows to significantly reduce the sensing layer thickness without loosing signal amplitude. As a result the magnetic flux is more concentrated, which further increases the sensitivity. Sensors for the HDD application –whether of GMR or AMR type– are laterally so small that despite of the thin film structure the demagnetization field plays an important role. For AMR sensors, demagnetization effects indeed limit the minimum track width. The smaller thickness of GMR type sensors allows to further decrease the lateral size, and the spatial resolution of the read-out can be improved. This is the main reason why on the route to storage densities beyond 100 Gbit/in$^2$ major hard-disk manufacturers have replaced AMR by GMR. The evolution of the width and thickness of the magnetoresistive

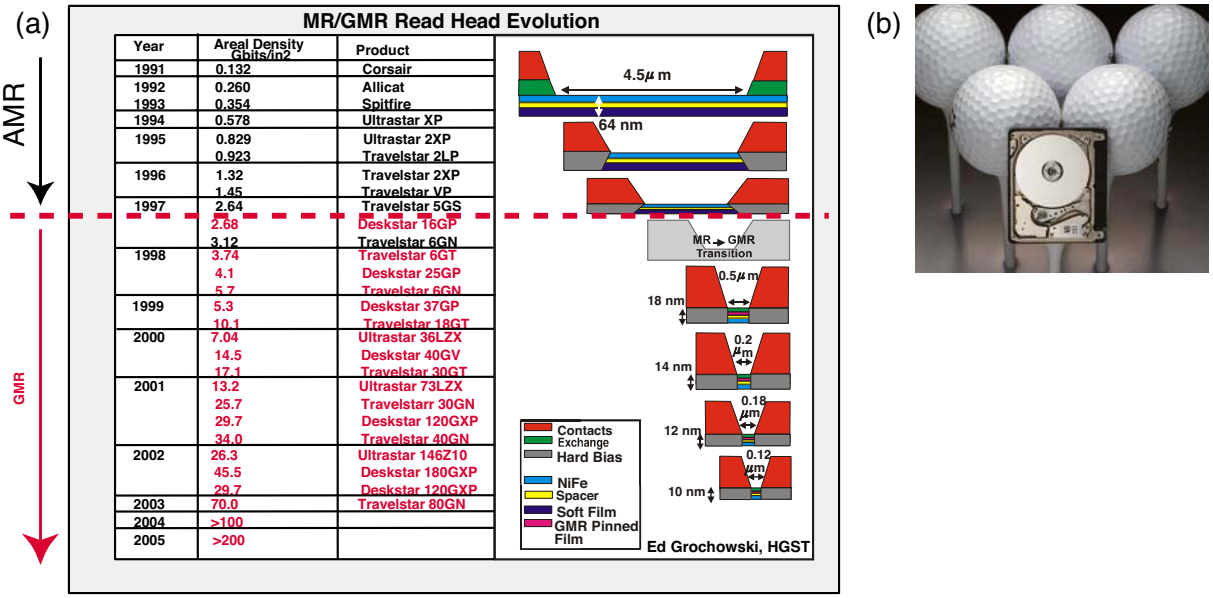


**Fig. 5:** *(a) The evolution of the dimensions clearly shows the transition from AMR to GMR sensor technology in 1997. (b) The 2006 version of the microdrive yields the following key specifications: 8 GByte data capacity, 1 inch disk diameter, 119 GBit/in$^2$ storage density, 16 gr weight, and 3600 rpm rotation speed.*

layers in read heads is shown in Fig. 5(a). The transition from AMR to GMR is evident. The so-called microdrive shown in Fig. 5(b) is an example of a device that is only possible due to the application of the GMR effect. It has a disk diameter of one inch (25.4 mm) and a storage capacity of 8 GByte. The storage density is 119 GBit/in$^2$ (specifications of the 2006 version, the corresponding values of the 2000 version, 340 MByte and 5 GBit/in$^2$, illustrate the fast-paced progress of magnetic data storage). For a comprehensible explanation of a GMR read head we refer the reader to the animation in Ref. [11].
Further realized or envisaged applications of the GMR effect are position and angle sensors for the automotive industry and automatization, magnetocouplers, strain sensors [12], GMR-based MRAMs [7], and biochips [13].

# 3 Spin-torque transfer (STT)

The GMR effect describes the fact that the alignment of the layer magnetizations in a trilayer controls the electric resistance, *i.e.* the current flow. According to Newton's third law "*actio* equals *reactio*" there should also exist an inverted effect, for which the current flow controls the magnetization alignment. Such an effect is of outmost interest as it represents a novel, alternative concept to induce magnetizations switching, in particular in nano-scale magnets.

## 3.1 Advanced magnetic switching concepts: Need and requirements

Magnetization reversal has become a fundamental issue of the physics of magnetic (nano)particles. The research field is driven by the needs of current and perspective technologies in magnetic data storage and spintronics. The magnetic random-access memory (MRAM) and patterned, ultra-high-density perpendicular recording media are examples, where small magnetic

elements have to be magnetically switched. Furthermore, most envisaged spintronic devices rely on spin-polarized currents generated or analyzed by ferromagnetic electrodes (*e.g.* ferromagnetic electrode of a spin-injection device). Control of these current polarizer and analyzer elements involves switching of their magnetizations.
The ever increasing clock frequencies in the above mentioned applications require switching on a timescale below 1 ns. Here, we deal with switching on a timescale of roughly 100 ps. Ultrafast magnetization dynamics on even faster timescales down to the fs-regime, which come into play when the electronic and hence the magnetic system is highly excited and driven away from the equilibrium by ultra-short, intense laser pulses, is currently the subject of intense research, but is beyond the scope of our experiment. As a further requirement, the switching processes should dissipate as little energy as possible in order to reduce the heat load on the devices and the power consumption of (battery-powered) equipment. Additionally, a clear potential for downscaling and compatibility with semiconductor technology are also criteria for competitiveness. All these requirements –speed, low energy dissipation, local addressing, scalability and integrability into semiconductor technology– demand for new and advanced magnetic switching concepts.
In the conventional approach, magnetization switching or reversal is triggered by applying an external magnetic field. As the structures get smaller and smaller it becomes increasingly more difficult to focus the external field to a single nanoobject. Therefore, one would prefer a switching scheme based on an electric current or voltage, which can be applied very locally.
The experiment "Spin Transport in Magnetic Nanostructures" deals with such an advanced switching concept, namely the current-induced magnetization switching. In this novel concept the transfer of spin momentum is employed to trigger a magnetization reversal or to excite magnetization dynamics in a nanomagnet.

## 3.2 Basics of magnetization dynamics

Comprehensive introductions to magnetization dynamics are given in many textbooks. The present section is intended to be a reminder and to define quantities and symbols used later on.
In the following, we assume that the amplitude of the magnetization attributed to a certain volume of magnetic material is constant. Therefore, the magnetization dynamics of interest within this volume can be described by the Landau-Lifshitz-Gilbert (LLG) equation of motion for magnetic moments in an effective field. In order to describe mesoscopic magnetic objects properly, micromagnetic simulations are employed: The object to be described is geometrically subdivided into small volume elements with a size smaller than the exchange length of the material (typically a few nm), within which the assumption of constant magnetization is justified. In the LLG equation of each element direct exchange with neighboring volume elements and the demagnetizing field due to all other elements are taken into account. The resulting set of coupled equations is solved by means of finite-element computer codes.
A magnetization $\vec{M}$ in an effective field $\vec{H}_{\text{eff}}$ gives rise to the energy density

$$E = -\mu_0 \vec{M} \cdot \vec{H}_{\text{eff}}. \tag{4}$$

Parallel alignment of $\vec{M}$ with $\vec{H}_{\text{eff}}$ yields the energy minimum, whereas antiparallel alignment corresponds to an energy maximum. This consideration is the basis of conventional magnetization switching, where an external field is applied in the direction of the desired final magnetization vector and, thus, usually opposite to the initial magnetization direction. However, the

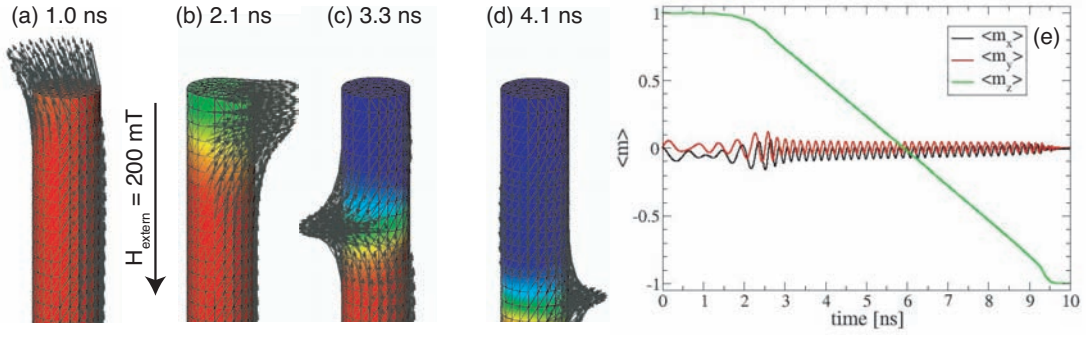


**Fig. 6:** *Micromagnetic simulation of the remagnetization of a Ni nanowire with a diameter of 40 nm and a length of 1 $\mu$m. The initial magnetization points along the $+z$-direction. At t=0, a field of 200 mT is applied in the $-z$ direction. (a)-(d) are snapshots after different time delays. (e) shows the evolution of the magnetization components averaged over the whole nanowire (denoted by $\langle m_{x,y,z} \rangle$). The oscillations of the $x$ and $y$ components reflect the precession of the magnetization in the domain wall. After [14].*

torque exerted on $\vec{M}$ is proportional to $-(\vec{M} \times \vec{H}_{\text{eff}})$. It vanishes when $\vec{H}_{\text{eff}}$ is applied antiparallel (or parallel) to $\vec{M}$. Obviously, for the antiparallel alignment the system is in an unstable equilibrium. Therefore, the switching process depends on perturbations (temperature, edge effects, magnetic inhomogeneities, *etc.*) making it slow, energetically inefficient, and spatially incoherent. An example is given in Fig. 6. The time evolution of the magnetization in a magnetic Ni nanowire exposed to an external field applied antiparallel to the initial magnetization is shown [14]. First it takes almost 1 ns for the magnetization distribution to significantly deviate from the initial state, which is close to the unstable equilibrium. The remagnetization starts at the the end of the nanowire by nucleating a domain with reversed magnetization (blue), which then expands by means of domain wall displacement. The magnetization in the domain wall (green) precesses and winds slowly down the nanowire axis. The full remagnetization takes almost 10 ns [Fig. 6(e)]. Thus, the result of the simulation shows that, in general, the conventional switching occurs in an incoherent fashion, thus leading to oscillations of the magnetization vector and to the formation spin waves.

Applying the effective field non-collinear to $\vec{M}$ gives rise to a non-zero torque, but it points perpendicular to $\vec{H}_{\text{eff}}$. The response of $\vec{M}$ is a precession around $\vec{H}_{\text{eff}}$. Only the presence of damping causes $\vec{M}$ to relax towards $\vec{H}_{\text{eff}}$ as required by the energy minimum of Eq. (4). The motion of the magnetization vector $\vec{M}$ in space is described by the Landau-Lifshitz-Gilbert (LLG) equation

$$\frac{1}{\gamma}\frac{d\vec{M}}{dt} = -\vec{M} \times \vec{H}_{\text{eff}} - \frac{\alpha}{M_{\text{S}}}\vec{M} \times (\vec{M} \times \vec{H}_{\text{eff}}), \tag{5}$$

where $\gamma$ is the gyromagnetic ratio, $\alpha$ the phenomenological Gilbert damping constant, and $M_{\text{S}} = |\vec{M}|$ the saturation magnetization.[1] The effective field $\vec{H}_{\text{eff}}$ is the sum of all fields acting on $\vec{M}$ and can be derived as the negative variational derivative of the total areal energy density $E_{\text{tot}}$ with respect to the magnetization

$$\vec{H}_{\text{eff}} = -\frac{1}{\mu_0}\frac{\delta E_{\text{tot}}}{\delta \vec{M}}, \tag{6}$$

[1] Other forms of the LLG equation can be found in literature, which use different definitions of the coefficients $\gamma$ and/or $\alpha$.

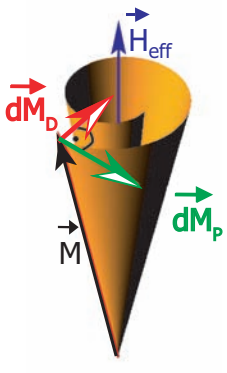


**Fig. 7:** *Motion of a magnetization vector $\vec{M}$ in an effective field $\vec{H}_{eff}$. The first term in Eq. (5) gives rise to the tangential torque $d\vec{M}_P/dt$ driving the precession and the second term $d\vec{M}_D/dt$ causes the damping.*

where $\mu_0$ is the permeability of vacuum. The total energy $E_{\text{tot}}$ comprises contributions from the exchange energy, anisotropy energy, stray field energy, and the Zeeman energy due to an external field. The first term in Eq. (5) describes the precessional motion of $\vec{M}$ about $\vec{H}_{\text{eff}}$, and the second term the damping, which forces $\vec{M}$ to relax to the lowest energy configuration, $\vec{M}||\vec{H}_{\text{eff}}$ (Fig. 7). The simulation in Fig. 6 is obtained by integrating Eq. (5) for each node of the finite element mesh. Direct exchange between neighboring volume elements and the demagnetizing field due to all elements are taken into account and enter for each node via $\vec{H}_{\text{eff}}$. Obviously, the temporal evolution of a remagnetization process is intimately related to the magnetization dynamics described by the LLG equation. Note that both terms in Eq. (5) have their own timescales. The precession period (given by the Larmor frequency) is determined by the effective field $\vec{H}_{\text{eff}}$. The stronger $\vec{H}_{\text{eff}}$, the higher the Larmor frequency. Typical frequencies for magnetic materials like Fe, Co, Ni, or permalloy are of the order of several GHz yielding precession periods $\tau$ of fractions of a nanosecond. The timescale of the damping term, on the other hand, is governed by the phenomenological damping parameter $\alpha$. Typical values $\alpha \approx 0.001$ result in relaxation times of several nanoseconds. Therefore, relaxation usually occurs over several precessional revolutions. The magnetization component along $\vec{H}_{\text{eff}}$ approaches exponentially $M_{\text{S}}$, and components perpendicular to $\vec{H}_{\text{eff}}$ show an exponentially damped oscillatory behavior, the so-called magnetic ringing.

## 3.3 Current-induced magnetization switching

In 1996 Slonczewski [15] and Berger [16] predicted that a spin-polarized current propagating into a ferromagnetic layer exerts a torque on the magnetization of the layer, due to the exchange interaction between the electrons and the local magnetic moments. In layered metallic systems with alternating magnetic and non-magnetic layers, a current flowing perpendicular to the plane of the layers (CPP-geometry) is polarized by one ferromagnetic layer and transfers spin angular momentum to another ferromagnetic layer, where the transferred momentum acts as a torque on the magnetization. This effect is called *spin-torque transfer*. For this torque to be sufficient to perturb the magnetization from equilibrium, large current densities ($> 10^7$ A/cm$^2$) are required. If two stable equilibria for the magnetization exist (*e.g.* due to an uniaxial anisotropy), the spin-torque transfer can switch the magnetization from one equilibrium position to the other. This process is called *current-induced magnetization switching* and does not require an external

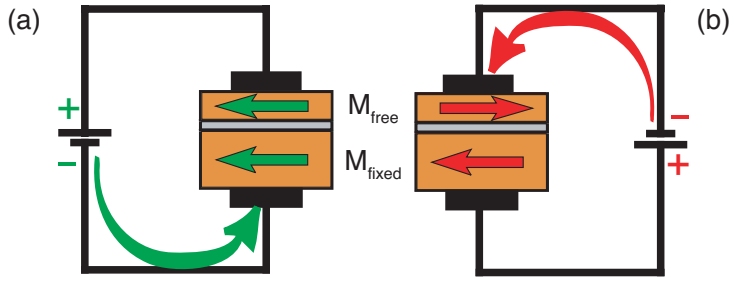


**Fig. 8:** *Phenomenology of current-induced magnetization switching: The stable alignment of the magnetizations depends on the polarity, i.e. the direction, of the current flowing perpendicularly through the trilayer.*

magnetic field to induce switching.

The phenomenology of current-induced magnetization switching is shown in Fig. 8. We consider two ferromagnetic layers separated by a non-ferromagnetic spacer with a thickness below its spin diffusion length. The ferromagnetic layers are different in such a way (*e.g.* thickness or coercive field), that one of them can be remagnetized more easily than the other. We distinguish the two layers in the following by calling them *free* and *fixed* and draw them as a thinner and ticker layer, respectively. When electrons flow[2] from the fixed to the free layer, the magnetization of the free layers aligns parallel to the magnetization of the fixed layer and this alignment is stabilized [Fig. 8(a)]. When the current direction is reversed, however, the antiparallel alignment is more stable and adopted [Fig. 8(b)] as will be explained in Sect. 3.4. Thus, a magnetization reversal can be induced by reversing the *polarity* of the dc current flowing through the layers.

An experimental arrangement for the observation of current-induced switching is displayed in Fig. 9(a) taken from one of the pioneering experimental papers in this field by the Cornell group [17]. The sample is a nanopillar consisting of a thin, free Co layer (Co 1) with a thickness of 2.5 nm and a thick, fixed Co layer (Co 2) of 10 nm thickness. The Cu spacer in between is 6 nm

[2] Whenever I refer in this lecture to the direction of a current, I mean the direction of the electron flux rather than the (opposite) technical current direction.

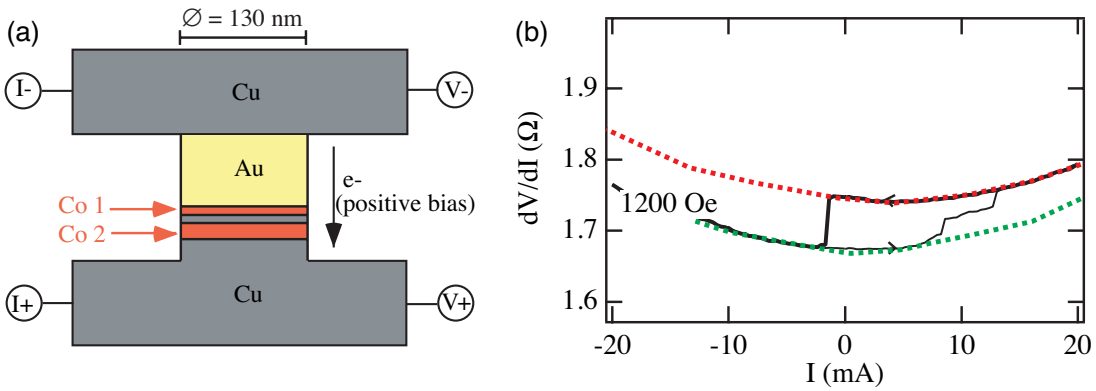


**Fig. 9:** *(a) Schematic pillar device with two Co layers (Co 1 and Co 2) separated by a 6 nm thick Cu layer. The pillar diameter is 130 nm. (b) The $dV/dI$ measurement as a function of the current through the column device yields the relative alignment of the magnetic layers via the GMR effect. After [17].*

thick and, thus, thinner than the spin diffusion length of Cu (about 100 nm). The lateral diameter of the pillar is only 130 nm. A current can be fed in by leads $I^-$ and $I^+$, and the voltage drop is measured at $V^-$ and $V^+$. The lateral restriction is required to obtain the necessary high current density (of the order of $10^7$–$10^8$ A/cm$^2$ corresponding to 1–10 mA in a 100 nm-diameter pillar) to establish a steady (constant current) non-equilibrium situation. The relative orientation of the Co layers can be measured via the GMR effect of the Co 1/Cu/Co 2 trilayer system. Figure 9(b) displays the differential resistance as a function of the applied current. At negative bias electrons flow from the fixed (thick) to the free (thin) Co layer and stabilize the parallel magnetization alignment which yields a low $dV/dI$. At positive bias the parallel alignment is destabilized, Co 1 switches to the antiparallel alignment at a sufficiently large current, and $dV/dI$ increases. Upon reducing the current [thick black line in Fig. 9(b)] hysteretic behavior is observed such that Co 1 switches back to parallel at a negative current. An external magnetic field is applied to define and fix the magnetization direction of the Co 2 layer. Note, that the curve shows hysteretic behavior with two different stable states at zero applied current. Therefore, positive and negative current pulses allow to switch between states at zero current with parallel and antiparallel magnetization alignments. This mechanism constitutes the basis for an advanced switching mechanism.

## 3.4 Physical picture of spin-torque transfer: Absorption of the transverse spin current component

Being aware of the high current densities, one might suppose that the Oersted field generated by the current is responsible for the switching behavior. However, the Oersted field has the wrong symmetry. Its circular field lines lie in the plane of the sample and favor in the steady state (*i.e.* state formed a long time after switching on the current) a vortex-like magnetization state with a direction of rotation depending on the current polarity. These vortex states would appear symmetrically for both current directions in clear contrast to the behavior in Fig. 9(b). Furthermore, the strongest Oersted field occurs at the pillar circumference and scales like $I/d$, where $I$ is the current and $d$ the pillar diameter. The spin-torque transfer effect, on the other hand, scales like the current density $I/d^2$. Therefore, the spin-torque transfer effect becomes stronger below a certain structure size $d_\mathrm{c}$. Theoretical estimates and available experiments suggest a $d_\mathrm{c}$ of the order of 100 nm. This fundamental size restriction fortunately coincides with the possibilities of e-beam lithography and at the same time yields the needed current densities at technically convenient current amplitudes [10 mA in an area of (100 nm)$^2$ correspond to about $10^8$ A/cm$^2$]. In practice one always has to be aware of the presence of the Oersted field and has to take its possible influence into account.

In order to develop a physical picture for the spin-torque transfer effects, we start by considering the fate of a polarized current that enters a ferromagnet from a metallic non-magnet. The situation is sketched in Fig. 10(a). The incident current is polarized along an axis tilted by the angle $\theta$ with respect to the magnetization $\vec{M}$ of the ferromagnet. For simplicity we assume a polarization axis in the drawing plane. In experiments, due to the shape anisotropy, the polarization axis is usually in the plane of the layers. The general arguments given below are valid for both cases. The (normalized) wave function of an incident, accordingly polarized electron can be written as a superposition of spin-up and spin-down components with respect to the quantization axis defined by $\vec{M}$. The amplitudes are $\cos(\theta/2)$ and $\sin(\theta/2)$, respectively, and correspond to a specific transverse component of the spin vector given by $\sin(\theta)$. At the interface to the ferromagnet the potential experienced by the electron changes and becomes spin-dependent. Inside

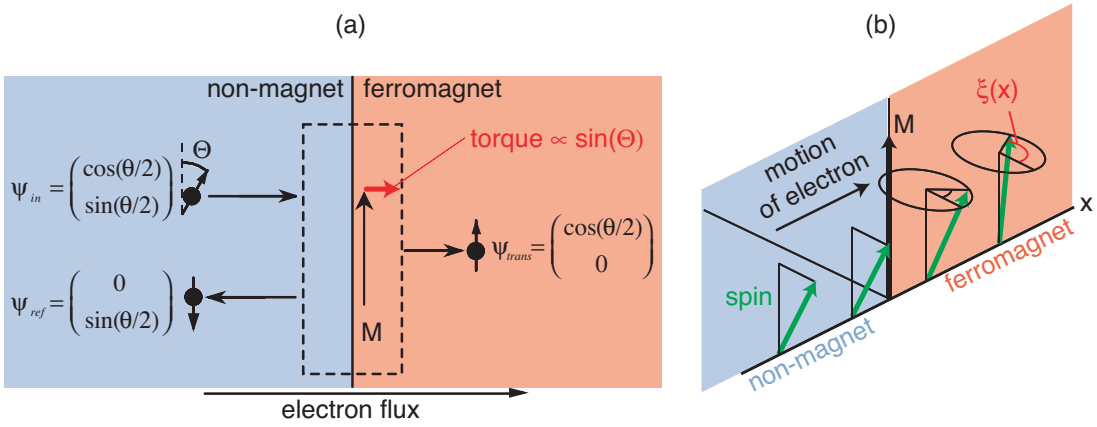


**Fig. 10:** *Two effects contributing to the absorption of the transversal spin current component in the interface region (dashed box) between a non-magnet and a ferromagnet. (a) Spin filtering: The incoming $\Psi_{in}$, transmitted $\Psi_{trans}$, and reflected $\Psi_{ref}$ wave functions (spinors) for the idealized case of perfect spin filtering are indicated. The absorbed transversal spin current is proportional to $\sin(\theta)$ and acts as a torque on the interface magnetization. (b) Spatial precession of the spin in the ferromagnet: The phase $\xi$ is constant in the non-magnet, but increases in the ferromagnet with distance $x$ from the interface.*

the ferromagnet this gives rise to the spin-split density of states. At the interface it also leads to spin-dependent transmission and reflectivity. Therefore, the transmitted and reflected wave functions are different superpositions of spin-up and spin-down components compared to the incident wave function. This leads unavoidably to different transverse spin components and, thus, to a discontinuity in the transverse spin current. The ”missing” transverse spin current is absorbed by the interface and acts as a current-induced torque on the magnetization. This effect occurs for each electron *individually* and is called spin filtering [15]. Figure 10(a) shows the spinors in the extreme case of perfect spin filtering. In realistic cases, roughly 50% of the transversal component is absorbed, and the transmitted as well as reflected currents still carry transversal components [18].

The actual *current polarization* of the transmitted and reflected currents is obtained by summing over the full distribution of conduction electrons. This introduces two additional effects. The first arises because the reflection and transmission amplitudes at the interface may be complex. This means that the spin of an incoming electron rotates upon reflection and transmission. The cancellation, which occurs when we sum over all these spin vectors, reduces the net outgoing transverse spin current. This is an entirely quantum mechanical phenomenon, for which there is no classical analog. A second effect arises because spin-up and spin-down components of an electron spinor on the have the same wave vector $k^{\uparrow} = k^{\downarrow} = k$ in the non-magnet but no longer when they are transmitted into the ferromagnet, $\Delta k = k^{\downarrow} - k^{\uparrow} \neq 0$. This is a consequence of the spin-split density of states. The two components are coherent, and a spatial phase $\xi(x) = \xi_0 + \Delta k x$ builds up [Fig. 10(b)]. This corresponds to a precession of the spin vector in space rather than time. The precession frequency is different for electrons from different portions of the Fermi surface. Therefore, when we sum over all conduction electrons, almost complete cancellation of the transverse spin occurs after propagation into the ferromagnet by a few lattice constants.

Taking all three effects –(i) spin filtering, (ii) rotation of the reflected and transmitted spin, and

(iii) spatial precession of the spin in the ferromagnet– together, to a good approximation, the transverse component of the transmitted and reflected spin currents are zero for most systems of interest (the completeness of the cancellations depends on the actual band structures). Thus, the incoming transverse spin current is absorbed by the interface and acts as a current-induced torque on the magnetization. A comprehensive theoretical treatment of these effects is given in Ref. [18].

Beyond these ballistic processes, spin-flip scattering in diffuse transport can also give rise to a transfer of angular momentum between the spin current and the lattice. But, there is only a net effect when the spin density deviates from the equilibrium spin density. In this case the relaxation process is associated with a net spin transfer. The difference between the actual and the equilibrium spin density is called *spin accumulation*. Spin accumulation occurs whenever a current crosses a region with unequal spin-dependent resistivities, *e.g.* $\rho_\uparrow < \rho_\downarrow$. In this example spin-down electrons accumulate in front of this region, and spin-up electrons prevail behind it. Again, if spin-flip scattering transfers a transverse spin momentum to the more localized electronic states (which form the magnetization $\vec{M}$), it will act on $\vec{M}$ like a torque [18, 19].

Up to now we have assumed that the incident current is polarized. In the experiment this can be achieved by a second ferromagnetic layer with a slightly tilted magnetization (angle $\theta$). This is possible when the two magnetic layers are separated by a non-magnetic spacer layer as shown in Fig. 11. The spin polarization process in this layer proceeds by the same mechanisms as described above. However, the polarization is *not* modified at the interface to the *non-magnetic* spacer layer because its density of states is *not* spin-split. The only requirement is that the spacer layer thickness is below its spin diffusion length to prevent significant depolarization by spin-flip scattering. Additionally, we reduce in Fig. 11 the extended ferromagnet of Fig. 10(a) to a thin film element and arrive at a situation very similar to the experimental setup of Fig. 9(a). In Fig. 11(a) the electrons flow from the fixed to the free layer. A current polarized by the fixed layer (1) hits the free layer and transfers its transversal component as a torque to the free layer. Part of the current is transmitted (2) and another part is reflected (3). This reflected

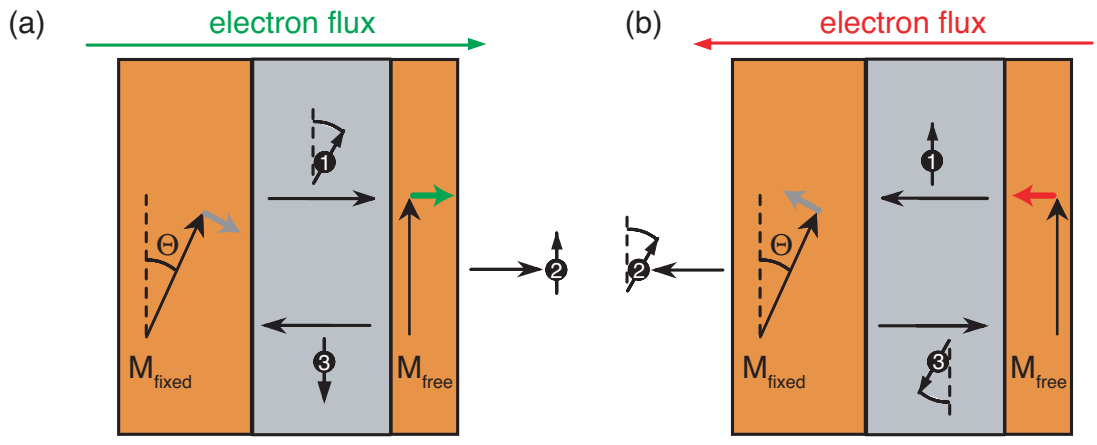


**Fig. 11:** *Physical picture of the current-induced magnetization switching. Orange regions represent the two ferromagnetic layers. Due to the assumed asymmetry $\vec{M}_{fixed}$ does not respond to the torque (short gray arrows) acting on it, whereas $\vec{M}_{free}$ can follow the torque (short green and red arrows). The numbers in the spins refer to the sequence of the description. (a) and (b) show the situation for opposite electron flux directions, which result in stable parallel or stable antiparallel alignment, respectively.*

current can now be considered as a polarized current impinging on the fixed layer. Again, the transversal component will be absorbed and acts as a torque on the fixed layer. However, due to the assumed asymmetry the fixed layer will resist to the torque, and only $\vec{M}_{\text{free}}$ starts to rotate in order to reach the stable parallel alignment with $\vec{M}_{\text{fixed}}$. For the opposite direction of the electron flux in Fig. 11(b), we obtain a similar situation but the torques point in the opposite directions. Therefore, the stable state corresponds to the antiparallel alignment of $\vec{M}_{\text{free}}$ and $\vec{M}_{\text{fixed}}$. Note, that in this case the torque on $\vec{M}_{\text{free}}$ arises from the current which first has been reflected from the fixed layer. Obviously, the asymmetry (fixed $\leftrightarrow$ free) plays an important role, which is very reasonable because "left" and "right" cannot be distinguished for the symmetric case.

## 3.5 Extended Landau-Lifshitz-Gilbert equation and critical currents

The torque acting on the free layer $d\vec{M}_{\text{free}}/dt$ has been calculated by Slonczewski [15] as

$$\frac{d\vec{M}_{\text{free}}}{dt} = \frac{g}{e}\frac{I}{A}\hat{M}_{\text{free}} \times (\hat{M}_{\text{free}} \times \hat{M}_{\text{fixed}}), \tag{7}$$

where $I/A$ is the current density, $e$ the electron charge, and $\hat{M}_{\text{free,fixed}} = \vec{M}_{\text{free,fixed}}/M_{\text{free,fixed}}$ are unit vectors. $g$ is a dimensionless and material-dependent coefficient describing the efficiency of the spin-torque transfer effect. The double cross product is indeed proportional to $\sin(\theta)$ and, thus, the absorbed transversal component of the spin current. The linear dependence on $I$ yields the reversed torque upon reversing the current direction. In order to study the influence of the spin-torque transfer effect on the magnetization dynamics the additional torque in Eq. (7) must be included into the LLG equation (5)

$$\begin{aligned}\frac{1}{\gamma}\frac{d\vec{M}}{dt} &= -\vec{M} \times \vec{H}_{\text{eff}} - \frac{\alpha}{M_{\text{S}}}\vec{M} \times (\vec{M} \times \vec{H}_{\text{eff}}) + \frac{g}{e\gamma M_{\text{S}}}\frac{I}{A}\vec{M} \times (\hat{M} \times \hat{M}_{\text{fixed}}) \\ &= -\vec{M} \times \vec{H}_{\text{eff}} - \vec{M} \times \left[\frac{\alpha}{M_{\text{S}}}(\vec{M} \times \vec{H}_{\text{eff}}) - \frac{g}{e\gamma M_{\text{S}}}\frac{I}{A}(\hat{M} \times \hat{M}_{\text{fixed}})\right].\end{aligned} \tag{8}$$

The subscript *free* is dropped for clarity. Obviously, the spin-torque transfer term has a form like the Gilbert damping, but depending on the sign of $I$ it can be negative or positive, see Fig. 12.

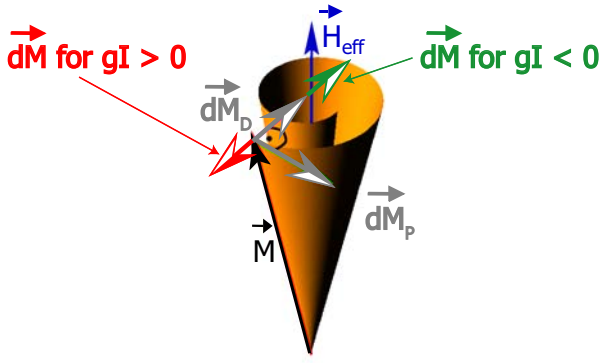


**Fig. 12:** *The torque due to the spin-torque transfer $d\vec{M}/dt$ can point along the Gilbert damping $d\vec{M}_D/dt$ or opposite to it. In the latter case it can destabilize $\vec{M}$ and induce switching (or microwave oscillations, see Sect. 3.6).*

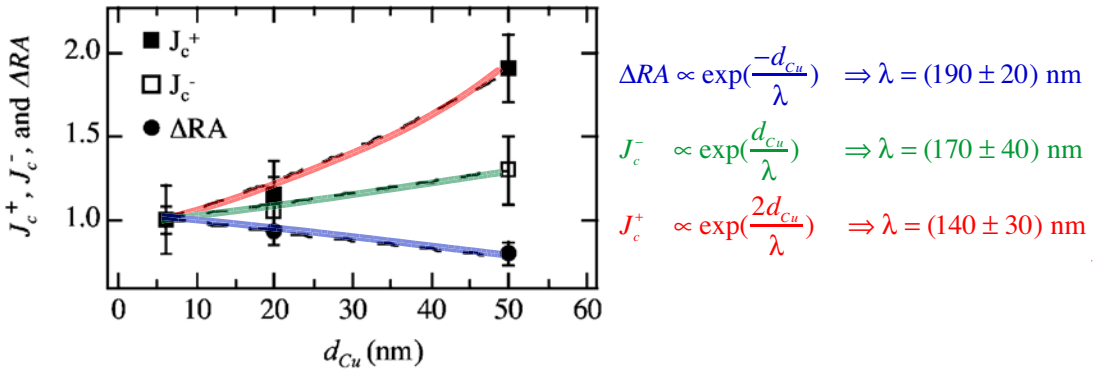


**Fig. 13:** *Normalized critical current densities $J_c^-$ (open squares), $J_c^+$ (filled squares), and magnetoresistance $\Delta RA$ (filled circles) of Co/Cu($d_{Cu}$)/Co nanopillars as a function of $d_{Cu}$. Dashed lines are fits to the exponential functions given on the right hand side. After [20].*

The latter case is more interesting, because the damping may be compensated by the spin-torque transfer term, and the precession amplitude is amplified, which leads to a destabilization of $\vec{M}$, *i.e.* switching or microwave oscillations (see Sect. 3.6). The critical current $I_c$ (or critical current density $J_c$) needed for switching can be derived from the condition that the spin-torque transfer term must exceed the Gilbert damping. The explicit expression for $I_c$ depends on details of the geometry, anisotropies, *etc.* and is not displayed here. In general the critical current density for switching from parallel to antiparallel alignment $J_c^+$ is different from the critical current density $J_c^-$ needed for the reversed switching direction.

Figure 13 displays the dependence of the critical current densities $J_c^\pm$ and the CPP-GMR times area product $\Delta RA$ of Co/Cu($d_{Cu}$)/Co nanopillars as a function of the spacer thickness $d_{Cu} = 6 \ldots 50$ nm [20]. All three quantities are normalized to their value at $d_{Cu} = 6$ nm. Due to the rather large spacer thicknesses one expects spin-flip scattering to play a role, at least for the largest $d_{Cu}$. CPP-GMR exponentially decreases like $\Delta RA \propto \exp(-d_{Cu}/\lambda)$, where $\lambda$ is the spin diffusion length of Cu at RT. The fit of the CPP-GMR data (solid circles) in Fig. 13 yields $\lambda = 190 \pm 20$ nm. Spin-flip scattering also reduces the spin-torque transfer efficiency $g$ in Eq. (7). Therefore, the critical current densities should increase with the total distance the electrons travel in Cu before they exert the switching torque on the free layer. According to Fig. 11(a) the electrons have to traverse the Cu spacer once from the fixed to the free layer to switch to the parallel state. Hence, $J_c^- \propto \exp(d_{Cu}/\lambda)$. For the switching to the antiparallel state, however, the electron travel first from the free to the fixed layer, where they are reflected, and then back to the free layer to induce the switching [Fig. 11(b)]. Hence, we expect for $J_c^+$ a factor of 2 in the exponent, $J_c^+ \propto \exp(2d_{Cu}/\lambda)$. The dashed lines in Fig. 13 are fits according to these expectations and yield $\lambda = 170 \pm 40$ nm for $J_c^-$ and $\lambda = 140 \pm 30$ nm for $J_c^+$. If the factor of 2 is not taken into account, the $J_c^+$ data yields $\lambda = 70 \pm 20$ nm, which is not in agreement with the values from the $\Delta RA$ and $J_c^-$ data. Therefore, this experiment nicely confirms the physical picture introduced in Sect. 3.4.

## 3.6 Current-driven magnetization dynamics

In all experiments discussed so far, the external field was lower than the coercive field of the free layer. Therefore, the presence of (uniaxial) shape or magnetocrystalline anisotropy gives rise to at least two stable states, and the current-induced torque can cause switching between

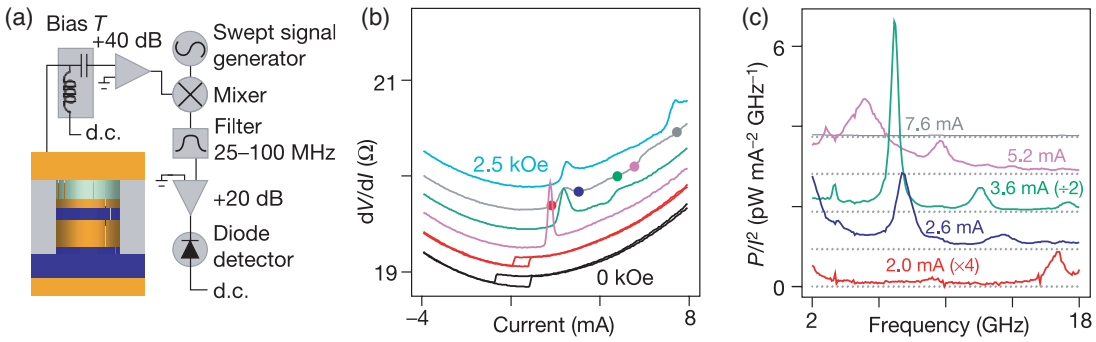


**Fig. 14:** *(a) Experimental setup for the measurement of the microwave signals generated by the spin-torque transfer in the nanopillar shown on the left side. (b) Differential resistance versus current for different fields. The hysteresis in the black and red curves vanishes for external fields exceeding the coercivity. Peaks appear instead. (c) Microwave spectra measured at 2 kOe [gray curve in (b)] at different current amplitudes as marked by colored dots in (b). After [21].*

these states. If the external field exceeds to coercivity, only one stable magnetization state exists, namely parallel to the external field. In this situation, the spin-torque transfer effect can decrease or increase the precession angle (see Fig. 12). The latter is the more interesting case because the free layer can be driven into new types of oscillatory magnetic modes, which are not attainable with magnetic fields alone. An example is large-angle precessional modes. Any oscillatory motion of the free layer with respect to the fixed layer results, due to the GMR effect, in a variation of the resistance. Therefore, the dc current that gives rise to the spin-torque transfer effect generates a time-varying voltage with typical frequencies in the microwave range. Figure 14(a) shows a measurement setup that allows direct electrical measurements of the microwave-frequency dynamics [21]. The microwave voltage signal is separated from the dc current using a bias-T and fed into a heterodyne mixer circuit, which basically acts as a spectrum analyzer for GHz frequencies. Figure 14(b) show resistance *versus* current plots, similar to Fig. 9(b), for different external fields. With increasing field (from bottom to top) the hysteretic behavior gives way for peaks. Microwave spectra taken under the current and field conditions marked in Fig. 14(b) by colored dots are displayed in Fig. 14(c). Rather sharp peaks at frequencies of several GHz are resolved. Figure 15(a) shows the rich

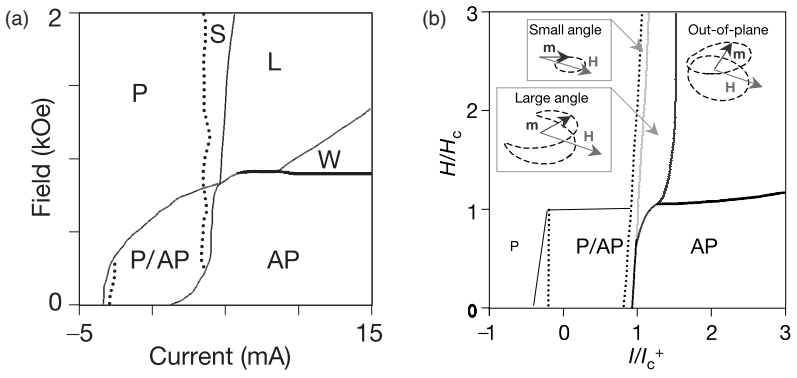


**Fig. 15:** *(a) Experimental and (b) calculated dynamic stability diagram. Different regions are explained in the text. Current and field axes in (b) are normalized to the critical current $I_c^+$ and the coercive field $H_c$, respectively. After [21].*

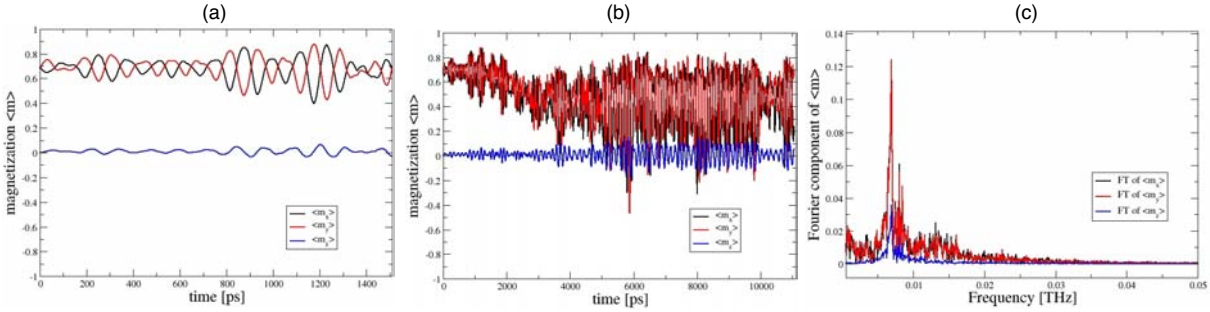


**Fig. 16:** *Simulated current-driven oscillations of the magnetization in a disc-shaped nanomagnet (d = 150 nm). After applying the current, the initial oscillations (a) quickly evolve into a noisy signal (b). At least one clear peak can be seen in the Fourier spectrum (c).*

dynamic stability diagram determined from such spectra. The basic features can be reproduced by numerically solving the extended LLG equation (8) for a macrospin, which is supposed to describe the complete free layer, as demonstrated in Fig. 15(b). $P$ and $AP$ stand for stable parallel and antiparallel alignment, and $P/AP$ is the region of bistability where hysteretic switching is possible. $S$ marks the small-amplitude precessional regime and and $L$ the large-amplitude dynamic regime. More simulations and calculated trajectories of stable precessional states can be found Ref. [22]. Region $W$ in Fig. 15(a) cannot be described by a macrospin simulation. Micromagnetic simulations beyond the Stoner-Wolfarth approximation have identified region $W$ to correspond to the formation and annihilation of dynamic vortices through the interplay of the current-induced Oersted field and the spin-torque transfer effect [23].

Figure 16 shows an example of a micromagnetic simulation of current-driven magnetization dynamics in an Fe disc of 150 nm diameter and 2 nm thickness. The sample is assumed to be monocrystalline with cubic magnetocrystalline anisotropy. If an external field of 50 mT is applied in the film plane, the magnetization in the disc is essentially homogeneous and aligned with the external field $H$. Due to the disc shape and the inhomogeneous demagnetizing field in any non-ellipsoidal particle, some small inhomogeneities occur at the perimeter of the disc. The magnetization of the disc is in a so-called onion state in order to reduce magnetostatic surface charges. $H$ is applied at 45° with respect to the easy axis and a polarized current with homogeneous current density $j = 5 \times 10^7$ A/cm$^2$ runs through the sample in perpendicular direction. The polarization direction of the current is parallel to one of the easy axes and encloses an angle of 135° with $H$ as sketched in Fig. 17(a). The dynamics of the magnetization can be monitored by plotting the volume-averaged normalized Cartesian components of the magnetization as a function of time. In the first 1.5 ns after switching on the electric current, only relatively small oscillations occur [Fig. 16(a)]. After about 3 ns, these small oscillations are soon replaced by a noisier signal. While the frequency of the oscillations remains conserved to a good extent, the amplitude varies strongly in a seemingly chaotic way [Fig. 16(b)]. The Fourier transform of this signal shows a sharp peak at about 7 GHz and some additional features at about 13 GHz, which are less pronounced [Fig. 16(c)]. Snapshots of the magnetic structure in the disc during this process are shown in Fig. 17. Surprisingly, the magnetization structures are very inhomogeneous and do not display any clear pattern. In contrast to this result, more well-defined features like resonant modes, spin waves or domain wall displacements usually occur in the case of ordinary, field-driven magnetization dynamics. These inhomogeneities can be attributed to the constant supply of energy provided by the electric current [22]. The system apparently converts

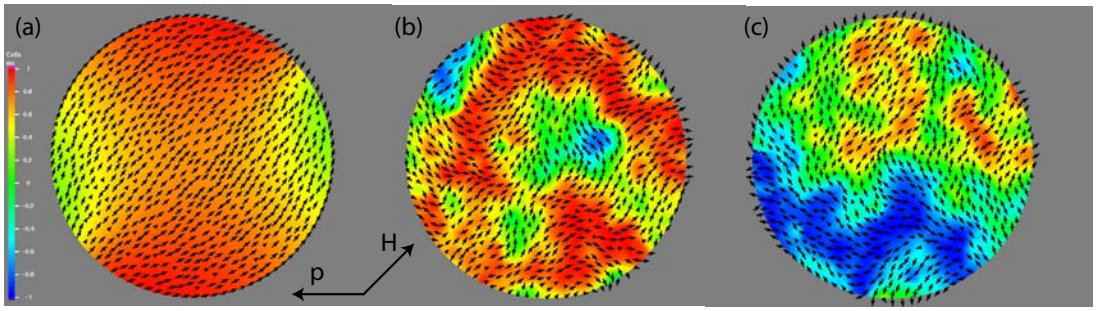


**Fig. 17:** *Typical snapshots of the simulated magnetic structure in the disc at different times after applying the current. (a): 0 ns; (b): 5.4 ns; (c): 8.3 ns. The magnetization structures are strongly inhomogeneous and are very dissimilar to structures known from field-driven magnetization dynamics. The directions of the current polarization $p$ and the external field $H$ are indicated.*

this energy into a large number of spin waves, which superimpose incoherently and lead to this type of noise [24]. The value of the intrinsic damping constant $\alpha$, which was set to 0.01 in this example, has a strong influence on the balance between energy dissipation and energy pumping [22, 24]. In spite of the pronounced magnetic inhomogeneities, the Fourier signal is remarkably clear in the sense that the average magnetization oscillates mainly at a well-defined frequency. It is reasonable to assume, that it is this dominant frequency that is measured experimentally [*e.g.* in Fig. 14(c)].
Simulations of this sort yield the following general conclusions: (i) The frequently used macrospin approximation is not applicable to describe the real dynamics of the magnetization. (ii) A clear signal in the frequency (as it is observed in experiments) does not necessarily result from a homogeneous spin precession. (iii) The magnetization dynamics induced by STT is qualitatively very different from the field-driven dynamics.
Nanomagnets driven by spin-polarized currents have the potential to serve as nanoscale, on-chip microwave sources or oscillators, tunable by field and current over a wide frequency range. These examples of recent developments demonstrate that the field of spin-torque transfer effects is rapidly evolving and bears the potential for further exciting physics, *e.g.* the realization of the magnetic analog of the injection laser. This device would provide *spin-wave amplification by stimulated emission of radiation*, and, accordingly, the name SWASER is already suggested [16].

# 4 Fabrication of nanopillars for STT measurements

As already mentioned in Sect. 3.4, the observation of STT effects requires small cross sections for the current flow in order to minimize the influence of the Oersted field and to obtain high current densities. As an example for the fabrication of samples with suitable properties, the preparation of single-crystalline Fe/Ag/Fe(001) nanopillars according to the process developed in Jülich [25] is introduced below.
In order to achieve single-crystalline growth the magnetic multilayers are deposited in a standard MBE system. The native oxygen layer of the GaAs(001) substrates ($10 \times 10\,\mathrm{mm}^2$) is desorbed by annealing for 60 min at $580^\circ\mathrm{C}$ under UHV conditions. We deposit 1 nm Fe and 150 nm Ag at $100^\circ\mathrm{C}$ to get a flat buffer system after annealing at $300^\circ\mathrm{C}$ for $1\,\mathrm{h}$. The Ag buffer

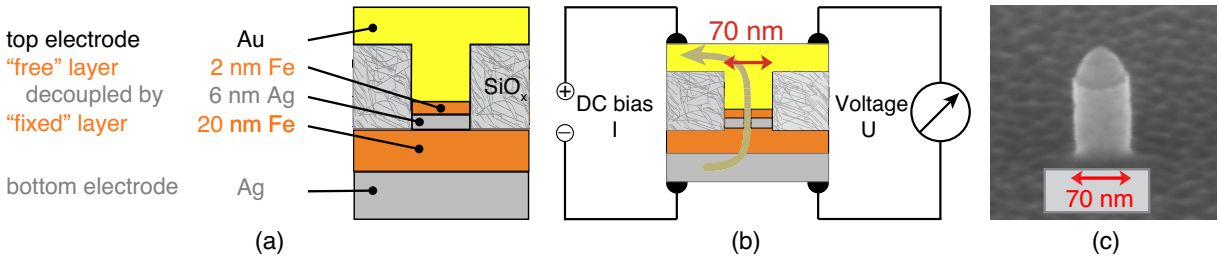


**Fig. 18:** *(a) Sequence, thicknesses, and functions of the layers within the multilayer stack. (b) Scheme of the junction geometry and the contacts for transport measurements. The dc current is confined to a diameter of $d \approx 70 - 150$ nm by the nanopillar. The voltage drop is measured across the pillar in 4-point geometry. (c) SEM micrograph of a free-standing nanopillar after ion-beam etching.*

also acts as a bottom electrode for the transport measurements [Figs. 18(a) and (b)]. The following layers are then deposited at room temperature: Fe(20 nm)/Ag(6 nm)/Fe(2 nm). We check the crystalline surface structure after each deposited layer by low-energy electron diffraction (LEED). The spots characteristic of (001) surfaces slightly broaden with increasing total thickness, but still indicate high crystalline quality, even for the final 50 nm Au(001) capping layer. Thicknesses are controlled by quartz crystal monitors.

In order to measure the STT effects in the CPP-geometry we have developed a combined process of optical and e-beam lithography. First, we define the leads and contact pads of the bottom electrode by using AZ5214 photoresist and ion beam etching (IBE) [Fig. 19(b)]. We then employ HSQ (hydrogen silsesquioxane) as negative e-beam sensitive resist and a Leica EBPG 5HR e-beam writer to define small nanopillars. The resist structures are circular and transferred into the magnetic layers by IBE [Fig. 19(c)]. The timed etching process is stopped inside the Ag spacer layer. Therefore, only the top, free FM layer [Fe(2 nm)] is confined to the pillar diameter

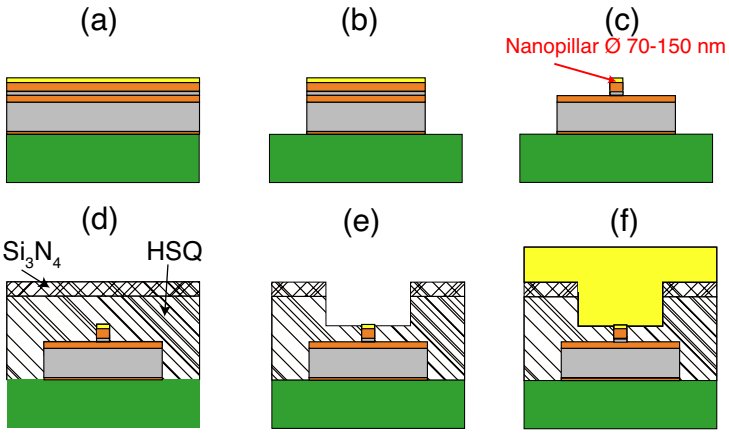


**Fig. 19:** *Lithographic process: (a) Extended epitaxial multilayer grown by MBE, (b) definition of 10 $\mu$m-wide bottom electrodes by optical lithography and IBE, (c) definition of nanopillars of 70-150 nm diameter by e-beam lithography and IBE, (d) planarization by HSQ and additional insulation by $Si_3N_4$; e-beam exposure converts HSQ into insulating $SiO_x$, (e) opening of a $10 \times 10\,\mu m^2$ window to the top of the nanopillar by IBE, and (f) definition of the top electrodes by optical lift-off. The colors of different materials correspond to those of Fig. 18.*

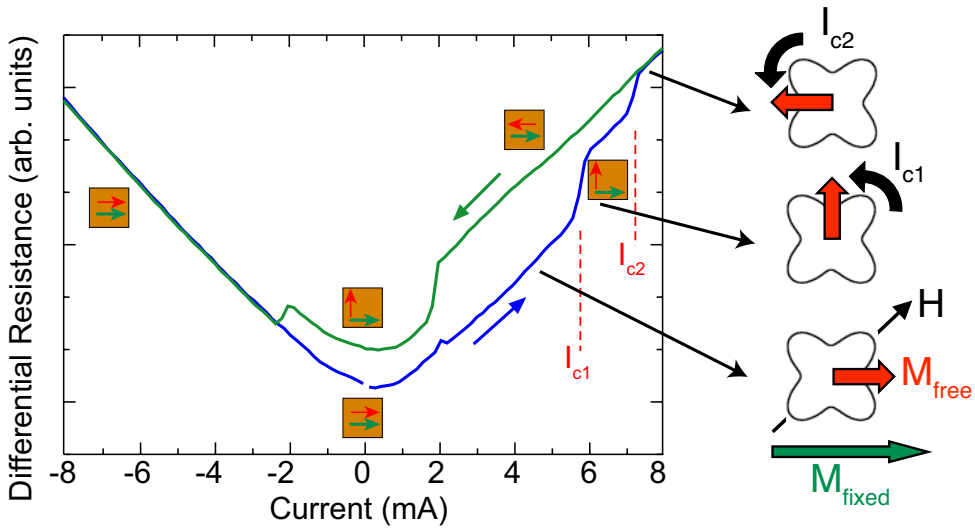


**Fig. 20:** *Two-step current-induced magnetization switching of a single-crystalline Fe/Ag/Fe(001) nanopillar measured at 5 K. The free layer magnetization switches first from parallel to perpendicular and then to antiparallel alignment relative to the fixed layer magnetization and vice versa for the decreasing current branch (green). A static magnetic field of 7.9 mT, which is weaker than the in-plane anisotropy field, is applied roughly along a hard axis.*

of 70 - 200 nm. The bottom, fixed FM layer [Fe(20 nm)] remains laterally extended over the with of the bottom electrode, which is of the order of 10 $\mu$m. The area underneath the pillar is coupled by direct exchange interaction to the extended part of the film, which makes it magnetically harder and less susceptible to current-induced STT with respect to the top Fe(2 nm) layer.

Typical dimensions of the developed resist structures are 50 - 150 nm (measured with an atomic force microscope). Due to redeposition of etched material during IBE, the nanopillars broaden to 70 - 200 nm. An SEM micrograph of the free-standing nanopillars in stage (c) of Fig. 19 is shown in Fig. 18(c). The pillars are planarized by spin-coating HSQ [Fig. 19(d)]. Subsequent e-beam exposure turns HSQ into $SiO_x$, which electrically insulates the pillars. In order to improve the insulation, especially at the side walls of the bottom electrodes, a 50 nm-thick $Si_3N_4$ layer is deposited by plasma enhanced chemical vapor deposition (PECVD). We open the top of the nanopillars by IBE and use an optical lift-off process of 40 nm Au for the preparation of the top electrode for the 4-point resistance measurements.

A typical measurement obtained from single-crystalline sample is shown in Fig. 20. In contrast to the data in Fig. 9(b) the switching occurs here in two steps via an intermediate resistance level. This two-step switching process arises due to the interplay between the four-fold magnetocrystalline anisotropy of the free Fe layer and the STT. At a positive current $I_{c1}$ the free layer starts to rotate with respect to the fixed layer. The anisotropy energy minimum at $90°$ stabilizes the the orthogonal state. Only at an even higher current $I_{c2}$ the local energy minimum is overcome and the free layer switches to the antiparallel alignment. Upon reversing the current, a similar behavior is observed. A detailed analysis of this data including the excitation of dynamic modes in the $90°$-aligned state can be found in Refs. [26, 27].

# Acknowledgment

I thank Saban Tirpanci for proofreading this manuscript.


# References


[1] J. M. Kikkawa and D. D. Awschalom, Nature **397**, 139 (1999).

[2] Review: A. Barthélémy, A. Fert, and F. Petroff, in *Handbook of Magnetic Materials*, edited by K. H. J. Buschow (Elsevier, Amsterdam, 1999), Vol. 12, Chap. Giant Magnetoresistance in Magnetic Multilayers.

[3] G. Binasch, P. Grünberg, F. Saurenbach, and W. Zinn, Phys. Rev. B **39**, 4828 (1989).

[4] M. N. Baibich, J. M. Broto, A. Fert, F. N. V. Dau, F. Petroff, P. Etienne, G. Creuzet, A. Friedrich, and J. Chazelas, Phys. Rev. Lett. **61**, 2472 (1988).

[5] P. Grünberg, R. Schreiber, Y. Pang, M. B. Brodsky, and H. Sowers, Phys. Rev. Lett. **57**, 2442 (1986).

[6] D. Dieny, J. Magn. Magn. Mater. **136**, 335 (1994).

[7] J.-G. Zhu, Y. Zhang, and G. A. Prinz, J. Appl. Phys. **87**, 6668 (2000).

[8] P. A. Grünberg, Sensors and Actuators A **91**, 153 (2001).

[9] Y. Sakuraba, K. Izumi, T. Iwase, S. Bosu, K. Saito, K. Takanashi, Y. Miura, K. Futatsukawa, K. Abe, and M. Shirai, Phys. Rev. B **82**, 094444 (2010).

[10] J. Barnaś, A. Fuss, R. E. Camley, P. Grünberg, and W. W. Zinn, Phys. Rev. B **42**, 8110 (1990).

[11] http://www2.fz-juelich.de/portal/lw_resource/datapool/_pages/pdp_1086/gmr.ram.

[12] H. J. Mamin, B. A. Gurney, D. R. Wilhoit, and V. S. Speriosu, Appl. Phys. Lett. **72**, 320 (1998).

[13] M. M. Miller, P. E. Sheehan, R. L. Edelstein, C. R. Tamanaha, L. Zhong, S. Bounnak, L. J. Whitman, and R. J. Colton, J. Magn. Magn. Mater. **225**, 138 (2001).

[14] R. Hertel, J. Magn. Magn. Mater. **249**, 251 (2002).

[15] J. C. Slonczewski, J. Magn. Magn. Mater. **159**, L1 (1996).

[16] L. Berger, Phys. Rev. B **54**, 9353 (1996).

[17] J. A. Katine, F. J. Albert, R. A. Buhrman, E. B. Myers, and D. C. Ralph, Phys. Rev. Lett. **84**, 3149 (2000).

[18] M. D. Stiles and A. Zangwill, Phys. Rev. B **66**, 014407 (2002).

[19] S. Zhang, P. M. Levy, and A. Fert, Phys. Rev. Lett. **88**, 236601 (2002).

[20] F. J. Albert, N. C. Emley, E. B. Myers, D. C. Ralph, and R. A. Buhrman, Phys. Rev. Lett. **89**, 226802 (2002).

[21] S. I. Kiselev, J. C. Sankey, I. N. Krivorotov, N. E. Emley, R. J. Schoelkopf, R. A. Buhrman, and D. C. Ralph, Nature **425**, 380 (2003).

[22] Z. Li and S. Zhang, Phys. Rev. B **68**, 024404 (2003).

[23] K.-J. Lee, A. Deac, O. Redon, J.-P. Nozières, and B. Dieny, Nature Materials **3**, 877 (2004).

[24] J.-G. Zhu and X. Zhu, IEEE Trans. Magn. **40**, 182 (2004).

[25] H. Dassow, R. Lehndorff, D. E. Bürgler, M. Buchmeier, P. A. Grünberg, C. M. Schneider, and A. van der Hart, Appl. Phys. Lett. **89**, 222511 (2006).

[26] R. Lehndorff, D. E. Bürgler, A. Kakay, R. Hertel, and C. M. Schneider, Phys. Rev. B **76**, 214420 (2007).

[27] R. Lehndorff, D. E. Bürgler, A. Kakay, R. Hertel, and C. M. Schneider, IEEE Trans. Magn. **44**, 1951 (2008).